APPLIED SCIENCES AND ENGINEERING

3D stretchable and self-encapsulated multimaterial triboelectric fibers

Chaoqun Dong[1], Andreas Leber[1], Dong Yan[2], Hritwick Banerjee[1], Stella Laperrousaz[1], Tapajyoti Das Gupta[1], Shahrzad Shadman[1], Pedro M. Reis[2], Fabien Sorin[1]*

A robust power device for wearable technologies and soft electronics must feature good encapsulation, high deformability, and reliable electrical outputs. Despite substantial progress in materials and architectures for two-dimensional (2D) planar power configurations, fiber-based systems remain limited to relatively simple configurations and low performance due to challenges in processing methods. Here, we extend complex 2D triboelectric nanogenerator configurations to 3D fiber formats based on scalable thermal processing of water-resistant thermoplastic elastomers and composites. We perform mechanical analysis using finite element modeling to understand the fiber's deformation and the level of control and engineering on its mechanical behavior and thus to guide its dimensional designs for enhanced electrical performance. With microtexture patterned functional surfaces, the resulting fibers can reliably produce state-of-the-art electrical outputs from various mechanical deformations, even under harsh conditions. These mechanical and electrical attributes allow their integration with large and stretchable surfaces for electricity generation of hundreds of microamperes.

INTRODUCTION

The fast development of wearable technologies has triggered a strong interest, both in academia and industry, to develop novel forms of efficient power systems beyond batteries, including energy harvesting from sunlight (*1*–*3*), heat (*4*, *5*), and movement (*6*). Among these developments, triboelectric nanogenerators (TENGs) have proven to be highly efficient to harvest low-frequency mechanical energy. Combined with unique attributes such as the potential for simple and low-cost fabrication schemes and an important materials and architecture flexibility, TENG devices have a great potential for impact in implants (*7*–*9*), robotics (*10*, *11*), sports (*12*, *13*), health care (*14*, *15*), and security (*16*, *17*).

A particularly emerging trend is to develop ultralight weight, large-area, low-profile, and unobtrusive TENG configurations (*6*), for the next generation of implantable probes (*18*), scaffolds (*19*), and wearable devices (*20*). Compared with standard two-dimensional (2D) devices, networks of advanced functional fibers represent ideal choices, allowing for highly complex and multimodal deformations, combined with breathability, robustness, and washability. Moreover, fiber technologies have evolved to the point where thin (submillimeter-diameter) fibers integrating different materials with complex micro- and nanostructures can be fabricated with high production yield. These advances have enabled the recent large-scale fabrication of high-performance display textiles and fiber lithium-ion batteries, which represent important achievement for smart electronic textiles and offer innovative ways to interact with electronic devices (*21*–*23*).

Thus far, however, the most advanced TENG structures combining high efficiency and robust output performance with the proper encapsulation, flexibility, and deformability could not be demonstrated in the fiber form. Current fiber-based TENG devices often operate in the single-electrode mode. This configuration is convenient to fabricate and use and can result in fibers with excellent elastic properties. However, existing systems lack an encapsulating body, which is indispensable for constructing a robust TENG configuration to avoid water vapor–induced deterioration of the triboelectric charges. This feature is imperative for harvesting energy under in vivo (*8*) and other complicated conditions (*24*), such as in the context of wearables and textiles. Moreover, single-electrode systems will see their output fluctuations depending on which materials they get into contact with, hence can be prone to unstable performance that is difficult to anticipate. Incorporating all the triboelectric active surfaces within a single device also ensures stable electrical outputs independent of material properties of the external mechanical sources, which can be an important requirement for self-powered sensing purposes.

Another commonly used configuration is the contact-separation mode, which alleviates the limitations mentioned above, but at the cost of fabrication complexity, which, in turn, markedly limit the performance of current contact-separation TENG fibers. These fibers are often composed of a cylindrical core-sheath structure with a gap between the inner core column and the outer sheath tube (*25*–*28*). Thus far, only very short lengths—generally at the scales of a few tens of centimeters—have been realized, by using multistep processing approaches that rely on coating, wrapping, and molding. These challenges have limited this design to laboratory scales, severely precluding their mass production and application. In addition, commonly used metallic wire–based electrodes are neither soft nor elastic, and even with the well-known serpentine configuration (*29*), the achieved mechanical deformability usually remains insufficient to meet the requirements for wearable applications. These fabrication challenges have also imposed severe limitations on the achievable device architectures, precluding progress in terms of performance and modes of mechanical actuation. Moreover, there has been a lack of focus on mechanical deformation modeling, partly because of the limited flexibility of the fabrication processes. Proper modeling is key to understanding and designing novel fiber devices with higher performance and robustness.

In this work, we alleviate the challenges associated with fabricating 3D TENG designs within ultrasoft and microstructured fibers,

[1]Institute of Materials, École Polytechnique Fédérale de Lausanne, 1015 Lausanne, Switzerland. [2]Institute of Mechanical Engineering, École Polytechnique Fédérale de Lausanne, 1015 Lausanne, Switzerland.
*Corresponding author. Email: fabien.sorin@epfl.ch

via innovative materials, processes, and modeling-based designs. Specifically, we demonstrate an advanced and robust triboelectric fiber composed of two stretchable and conductive nanocomposite materials with microstructured surfaces, separated by a large air gap and surrounded by a water-repellent elastomeric cladding. We show that thermal drawing can be used to produce the targeted fibers with thin, uniform, and complex cross-sectional structures in a scalable, simple, and precise way. We first design the fiber architecture by relying on finite element modeling (FEM) that enables a deeper understanding of the mechanical deformation of the fiber system. Operating in the contact-separation mode, the fiber can reliably generate electricity from reversible compression and stretching, even under the harsh conditions of humidity or repeated cycling. Aligning a 10-m-long fiber on a large and stretchable surface, we demonstrate the fiber's robust and reliable mechanical and electrical output performance triggered by various levels of compression and output currents of up to hundreds of microamperes. The innovative triboelectric fiber designs, materials, and processing strategy establish an innovative yet scalable approach to realizing robust and efficient TENG systems within soft and wearable constructs, paving the way toward novel devices and applications in health, personal care, and wearable devices.

RESULTS

Scalable fabrication of advanced stretchable TENG fibers

In Fig. 1 (A to C), we show the typical 3D fiber design that we propose, which exhibits a rectangular cross section composed of two asymmetric triboelectric parts that are separated by an air gap. The whole

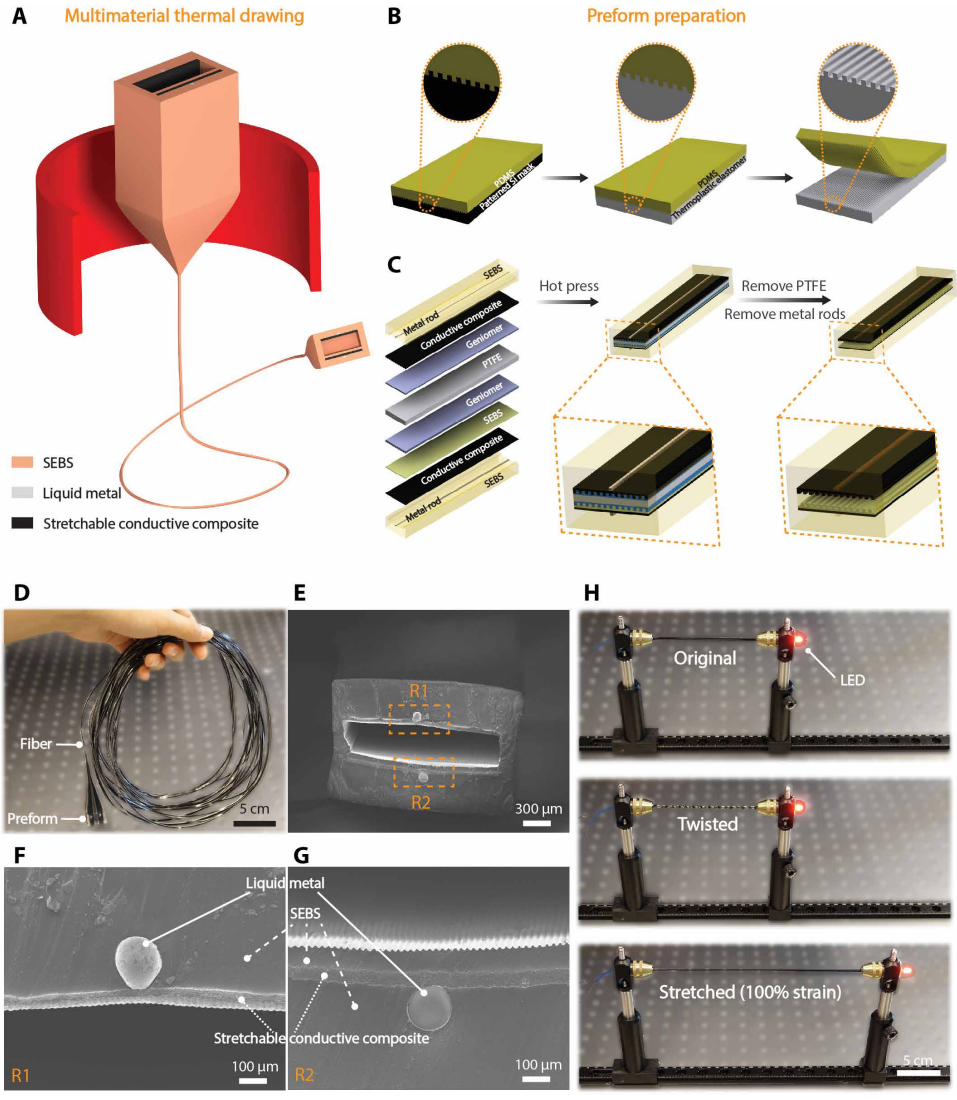

Fig. 1. Fabrication and structure of the stretchable, self-encapsulated fiber power system. (**A**) Schematic showing the thermal processing of a multimaterial preform into long fibers. (**B**) The preparation procedures of microtextured thermoplastic elastomers from a patterned mask. (**C**) Schematic showing the detailed structure and fabrication of the preform. The zoom-in illustration highlights the microtextured surfaces. (**D**) Photograph of a continuous 10-m-long fiber, showing the scalability of the fabrication process. (**E** to **G**) Scanning electron microscopy (SEM) images of fiber cross sections with microtextured inner surfaces. All necessary functional materials for electricity generation are fully encapsulated within a soft SEBS cladding. (**H**) Photographs of a 10-cm-long fiber being twisted or stretched to 100% strain with intact structure and consistent electrical conductivity, as indicated by the same brightness of a connected light-emitting diode (LED) that is powered through the two electrodes of the fiber.

structure is encapsulated within a thermoplastic elastomeric cladding [poly(styrene-*b*-(ethylene-*co*-butylene)-*b*-styrene) (SEBS)]. A stretchable and conductive composite forms the main electrode material. The rheological properties of such composites allow to draw it in a rectangular shape, hence increasing the surface area and generated charges, to optimize the output. An extra liquid metal channel is added to interface the composite to increase the electrodes' overall electrical conductivity along the fiber axis and thus reduce energy loss.

The fabrication approach that we propose relies on the preform-to-fiber thermal drawing technique, which is the conventional industrial approach to fabricating optical fibers (*30*–*34*). The whole process starts from the making of a multimaterial preform—the macroscopic version of the targeted fiber: Thermoplastic elastomer and conductive composite granules are first hot-pressed into slices with predefined microstructures and geometries and then assembled and consolidated into an assembly (Fig. 1, B and C) (see Materials and Methods for more details). The preform is then fed into a closed furnace and locally heated over the materials' glass transition temperatures and continuously pulled into thin and long fibers (Fig. 1A and movie S1). The process is scalable, allowing the production of uniform fibers with extended lengths (Fig. 1D). Despite the complex architectures integrating different materials and large hollow channels, the resulting fibers maintain the same structure as the initial preform after drawing (Fig. 1, E to G). In Fig. 1H, we illustrate the fiber's mechanical resilience and good electrical conductivity of the soft nanocomposites even under complex deformations such as twisting or large-strain elongation.

FEM of the mechanical deformation

To gain a predictive understanding of the mechanical deformation that triggers electrical outputs, we performed FEM on the fiber structure using the commercial software package Abaqus/Explicit (see Finite element modeling section in Materials and Methods and fig. S1 for details). Our simulation was first validated by comparing the predicted mechanical response of a fiber against the experiments. Figure 2A shows the excellent agreement between simulation and experiments for the applied pressure versus the compressive displacement of the fiber, defined as the change of distance between the top and bottom surfaces (i.e., change in height). The mechanical response of our triboelectric fiber can be divided into two regimes: before and after the top and bottom parts establish contact.

In the same figure, we provide the distributions of the maximum principal logarithmic strain of the fiber cross section (predicted by FEM) at five representative states during compression, including the initial stress-free state (i). At low pressures, the entire applied force is undertaken by the two side walls of the open channel (ii). As the pressure increases, the two side walls bend progressively and eventually induce the first contact between the top and bottom surfaces of the open channel. Because the two surfaces bend toward the inner side of the channel, the subsequent gradual increase in contact area leads to the smooth transition region in the loading curve. Maps (iii) and (iv) are captured, respectively, at the moments of the first contact and full contact. From FEM, we find that the first contact occurs at the pressure level of 160 kPa and compressive displacement of 322 μm, which agrees well with the experimental results. With further loading, the deformation is dominated by the compression of the SEBS body and the bending of the two side walls (v), resulting in a substantial increase in the stiffness of the structure, as indicated by the increase in the slope of pressure versus compressive displacement curve. Note that the maximum principal logarithmic strain associated with this loading process reaches values as high as +1.09 and −0.84 (positive and negative signs correspond to tensile and compressive strains, respectively). These large strains reiterate the necessity of using the SEBS elastomer as the main material, rather than common thermoplastic materials, which cannot withstand these high levels of reversible deformation. The simulated maximum principal logarithmic strain of the fiber during the whole loading process is recorded in movie S2.

The validated FEM enables us to quantitatively analyze the effects of fibers' dimensions on their mechanical behavior. Among various geometric features, we anticipated that the width and height of the open channel play key roles in the trigger pressure and compressive displacement at the first contact of the two inner surfaces. Therefore, we first varied the width of the channel x_1 while keeping other dimensions unchanged. Figure 2B shows the pressure-displacement curves of structures with different channel widths. As x_1/x_0 varies from 0.5 to 0.95 (x_0 is the width of the whole structure), the side walls become thinner, thereby reducing the stiffness of the structure before the first contact, as indicated by the decreased slopes. We quantified the pressure level and the compressive displacement at the contact point for varied x_1/x_0 in Fig. 2C. The trigger pressure decreases linearly with x_1/x_0, while the corresponding compressive displacement is constant because the height of the channel is fixed. Therefore, for the target TENG application, we should fabricate fibers with higher values of x_1/x_0 because such a design can provide higher contact surface area and require a lower trigger pressure to induce charge transfer between the tribosurfaces.

We also quantitatively investigated the effect of the height of the channel y_1 on the fibers' mechanical response. The loading curves of fibers with y_1/y_0 (y_o is the height of the whole structure) ranging from 0.05 to 0.35 are shown in Fig. 2D. Because the thickness of the side walls is fixed, the curves exhibit nearly the same shapes before contact. In Fig. 2E, we plot the compressive displacement at the contact point, determined by the height of the channel, thus linear to y_1/y_0. The trigger pressure in Fig. 2E is much less sensitive to y_1/y_0 compared to its variation with x_1/x_0 reported above (Fig. 2C). The nonlinearity of the trigger pressure may be due to the transition of deformation mode from compression to bending of the side walls, which become increasingly slender by increasing y_1/y_0. As discussed below, TENG devices with a large distance between the two surfaces would yield a better output performance. Therefore, guided by the FEM results, we chose to design and fabricate fibers with relatively larger x_1/x_0 and y_1/y_0 to obtain higher electrical outputs without the necessity of higher levels of trigger force and thus to achieve higher working efficiencies.

Material identification and microstructure engineering

Aside from the mechanical design to optimize electrical output, encapsulation is another key element to consider yet often ignored. It has been shown that moisture can drastically eliminate triboelectric charges on dielectric surfaces, largely impairing the output performance of TENG devices and even leading to almost no output at high relative humidity (RH) (*35*, *36*). In particular, Wang and colleagues (*37*) showed that a single drop of liquid water on one electrode of a contact-separation mode TENG device diminished a 70-V output to nearly zero. The fully encapsulated fiber architecture in this work is designed to be water resistant and capable of sustainably generating electricity even in a harsh environment. In addition

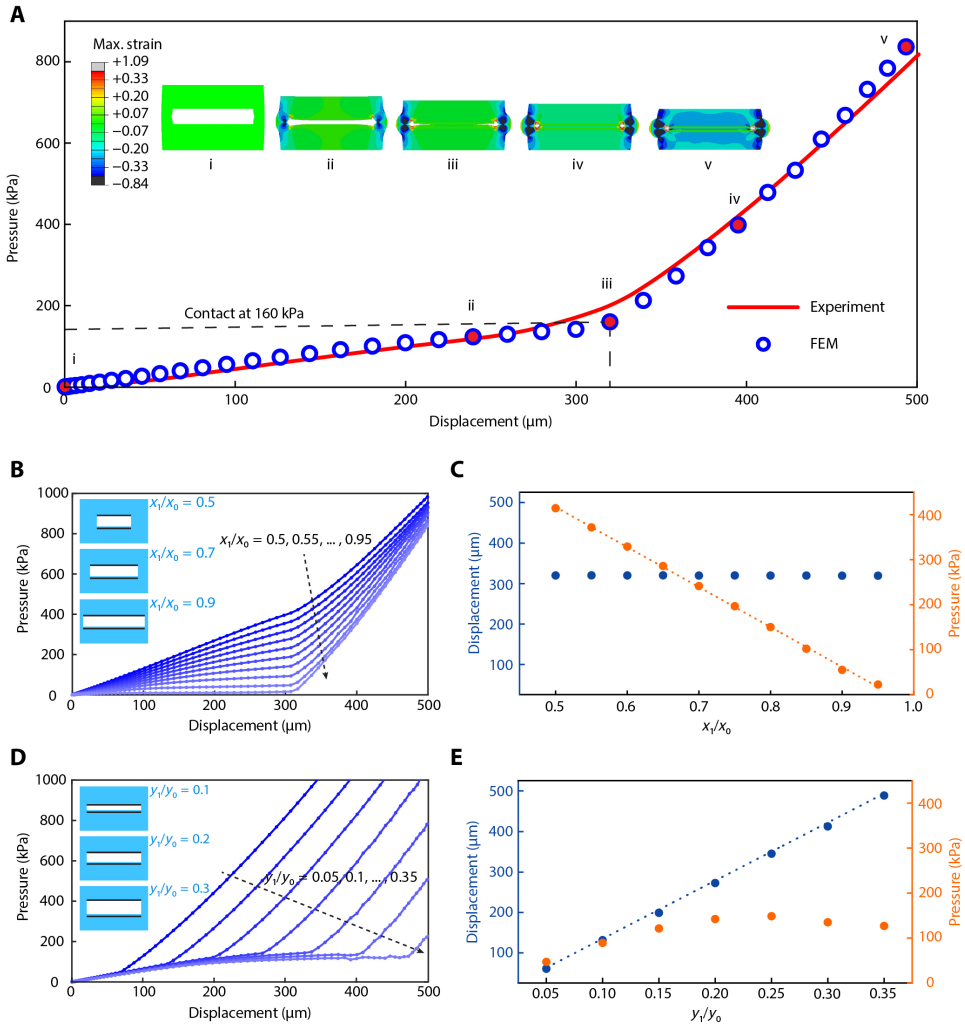

Fig. 2. FEM of the deformation of the fiber cross section. (**A**) Comparison of the mechanical response of the compressed fiber structure obtained through experimentation and FEM: pressure versus displacement. Insets present the simulated maximum principal logarithmic strain distributed in the fiber cross section during compression. The corresponding pressures and compressive displacements are indicated in the loading curve labeled by red dots. (**B** to **E**) Effects of variations of the width and height of the open channel on the mechanical behavior of the fiber. (B and D) Loading curves for fibers with varied width [in (B), x_1/x_0 ranging from 0.5 to 0.95, $y_1/y_0 = 0.23$] or height [in (D), y_1/y_0 between 0.05 and 0.35, $x_1/x_0 = 0.8$]. Note that the other dimensions are fixed and identical to those of the fiber sample tested in the experiment shown in (A). (C and E) Extracted values of pressure and compressive displacement as the top and bottom surfaces surrounding the channel come into contact. Schematics of initial fiber configurations with varying x_1/x_0 and y_1/y_0 are shown in the insets of (B) and (D), respectively.

to a proper structure, the interactions of the encapsulating material with water molecules, in both liquid and vapor forms, also play a key role in determining the RH that the device can sustain. We selected SEBS as the encapsulating material because of its hydrophobicity (Fig. 3A), high deformability, proper rheological behaviors that are compatible with thermal drawing, and good adhesion with a variety of other processable materials (*38*). To assess the ability of SEBS to resist the diffusion of water vapor molecules, we measured the water vapor transmission rate (WVTR) of ~200-μm-thick SEBS films through a water vapor transmission tester. The average values of WVTR at the temperatures of 15°, 25°, 35°, and 45°C are 0.23, 0.555, 1.055, and 2.315 g/m^2 per day, respectively. Normalizing with the sample thickness yields the WVTR values of 0.046, 0.111, 0.211, and 0.463 g·mm/m^2 per day, respectively. We find that the values of SEBS are lower than most of the listed polymers and, in particular, 100 times lower than commonly used polydimethylsiloxane (PDMS), making it an excellent barrier to water penetration (*39*). We ascribe this property to the contribution of the hard styrene segment in SEBS, based on previous studies on block copolymers that suggested the inhibition effects of the hard segment on gas permeability (*40*, *41*).

In addition, the experimental WVTR results for SEBS show that the permeability is enhanced with increased temperature. This is due to the enhanced motion of the polymer segments and the increased energy of the water molecules at a higher temperature, which concurrently contribute to the accelerated diffusion of water vapor through the film (*42*). Such a temperature dependency of WVTR was evaluated using an Arrhenius relationship

$$\mathrm{WVTR} = \mathrm{WVTR}_0 \exp(-E_p/RT) \quad (1)$$

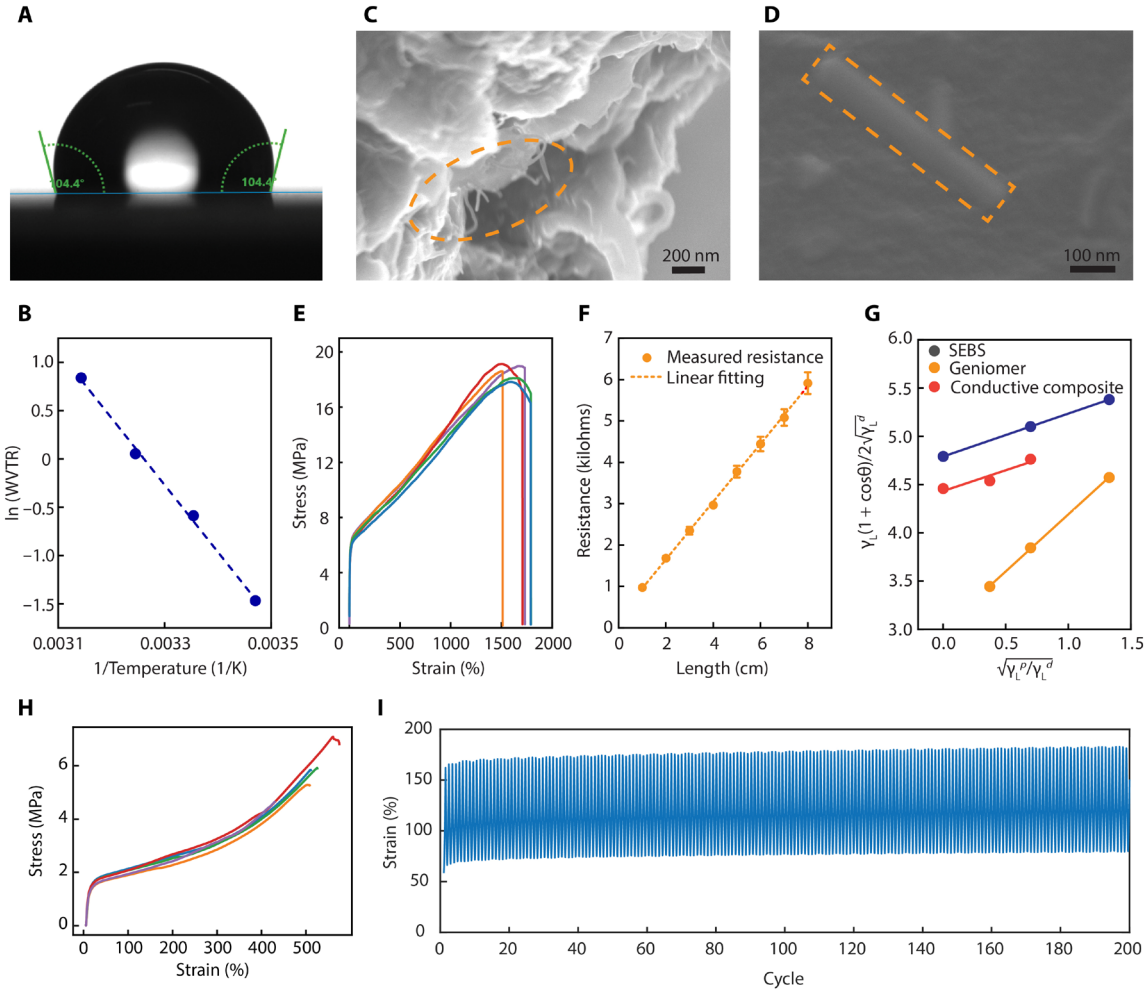

Fig. 3. Materials selection and characterization. (**A**) A water drop on a SEBS film showing the contact angle of approximately 104.4°. (**B**) The logarithm of WVTR values of SEBS as a function of the reciprocal of absolute temperatures (1/*T*) for the extraction of its permeation activation energy. (**C** and **D**) SEM images of the stretchable and conductive composite film, indicating the distribution and dimensions of the CNT fillers. (**E**) Stress-strain curves of the conductive composite before thermal drawing. (**F**) Measurement of the resistance versus length showing their linear relationship results from the overall homogeneous distribution of CNTs. (**G**) Surface tension studies of the involved polymers in this work. The data are extracted from a series of contact angle measurements. (**H**) Stress-strain curves of the energy harvesting fiber devices. (**I**) Dynamic mechanical tensile test of a fiber being stretched over 200 cycles under the applied forces in the range of 0.1 to 1.1 N.

where $WVTR_0$ is a preexponential factor, E_p is the activation energy of permeation that defines the energy barrier to be overcome for water vapor to permeate through the film, R is the universal gas constant, and T is the absolute temperature. By plotting the logarithm of WVTR versus $1/T$, E_p can be determined from the slope of the linear fitting in Fig. 3B. The resultant value is 57.7 kJ/mol, which is even higher than some hard polymers, including low-density polyethylene (33.5 kJ/mol), polypropylene (42.3 kJ/mol), and polyvinyl chloride (22.9 kJ/mol) (*42*). The above analysis confirms that the SEBS can be a good encapsulating material for stretchable electronic devices.

Let us now turn to suitable electrode materials. For stretchable fiber–based TENG devices, it is particularly important to integrate a conducting component that gathers features of high elasticity, good electrical conductivity, and compatibility with the required rheological properties for thermal drawing to optimize both geometrical design and electrical output. For contact-induced triboelectrification, we also need a large area electrode that comes into contact with the SEBS layer. On the basis of previous experiences drawing thermoplastic nanocomposites (*43*, *44*), our strategy is to use elastomer composites filled with carbon nanotube (CNT) fillers. The scanning electron microscopy (SEM) images of the composite before and after drawing are shown in Fig. 3 (C and D) and fig. S2. The diameter of the CNTs ranges from 25 to 55 nm, and the local dispersion of the CNTs in the matrix is relatively homogeneous, despite the formation of a few CNTs agglomerates. This aggregation is inherent if there is no extra physical or chemical treatment on the fillers due to their high aspect ratios and large surface area and the resulting high intrinsic van der Waals interactions between the tubes (*45*). The composite at the predrawing state can sustain a large strain of 1563%, with an average tensile strength of 18 MPa and Young's modulus of 115 MPa (Fig. 3E). To evaluate the distribution of CNTs, we performed resistance measurement of a 10-cm-long sample using a four-probe setup and collected data as the distance between the two signal collecting probes varied (Fig. 3F). The results reveal a linear relationship between resistance and position of the contact, suggesting a uniform electrical conductivity, hence the

distribution of CNTs, of the composite along the entire length. The resistivity extracted from this measurement is 0.2 ohm·m.

The amount of charges on polymer surfaces induced by the contact-electrification effect largely depends on the materials' surface area. Hence, microstructure engineering of the triboelectric surfaces to form a larger surface is important for higher output performance of TENG devices. We, therefore, exploited the versatility of the thermal drawing process to integrate surface microtexture (Fig. 1, A and C). Fabricating first at the preform level, we must be careful of the reflow mechanism driven by surface tension during drawing, which can cause the distortion or even collapse of the textures in the produced fibers (*19*, *46*). In general, thermoplastic materials with high mechanical strength can be directly processed at high viscosity to reduce reflow. However, this strategy is not applicable for thermoplastic elastomers because they have a very low mechanical strength of only several megapascals and hence must be drawn at relatively low viscosity to avoid breakage. In fig. S3, we show SEM images of a fiber produced from a preform with surface textures of 100 μm. It is clear that the microtextures have almost disappeared. Therefore, we must introduce a sacrificial material to form an intimate contact with the textured polymer in the preform, potentially leading to a significant reduction of the interfacial tension and thus lowering the driving force behind reflow during thermal drawing. The sacrificial layer can be mechanically removed afterward in a straightforward way given the bad adhesion between the Geniomer and SEBS polymers (*19*, *38*). We thus performed surface tension studies of the involved elastomers in the designed fibers (Fig. 3G). As described in more detail in the Supplementary Text and fig. S4, the interfacial tension between SEBS and Geniomer is much lower than the surface tension of SEBS alone. The same effect applies to the composite electrode and Geniomer. This analysis indicates that Geniomer is a suitable sacrificial layer for the proposed fiber design to significantly reduce thermal reflow during processing and to maintain the targeted microstructure as shown in Fig. 1 (E to G).

With this analysis, the structure presented in Fig. 1 can be described more precisely. It is composed of two microstructured triboelectric components separated by an air gap. Both components include a layer of stretchable composite, with one having an extra top layer of SEBS to generate and maintain separated triboelectric charges. We also integrated a liquid metal channel on the back of each composite electrode (Fig. 1, F and G) to ensure a good electrical conductivity along the fiber axis while not impairing its deformability. The stress-strain curves show that the fiber devices can maintain their mechanical integrity for strains up to around 500% (Fig. 3H). We also evaluated their mechanical behavior under cyclic loading. A fiber was repeatedly stretched and relaxed with a controlled force ramp between 1.1 and 0.1 N for 200 cycles, which can induce large strains between 60 and 180% (Fig. 3I). While the deformation slightly increased during the first 20 cycles, it remained stable for all the remaining cycles. We also quantitatively assessed the fiber's electromechanical behavior by subjecting it to repeated compression and stretching while simultaneously measuring the resistance of the electrodes. The stable electrical signals throughout the cyclic tests confirm the reliability of the fiber's electrical circuit (fig. S5).

Energy harvesting from compression and stretching

Having discussed the fabrication and characterizations of the mechanical and electrical properties, we now turn to evaluate the fibers' potential to work as TENG devices. Unlike the common dielectric-to-dielectric contact-mode systems, this fiber works in the conductor-to-dielectric mode, where the conductive composite functions as both the triboelectric layer and the electrode. The electricity-generating process of TENG devices is based on the coupling effects of contact-induced electrification and electrostatic induction caused by the triboelectric charges. We schematically illustrate this mechanism in fig. S6 and discuss it in detail in the Supplementary Text. The electric potential distribution of the fiber system was simulated via finite element simulation using COMSOL. A 2D finite element model was built to simplify the computation based on the fibers' cross-sectional dimensions and material properties. The SEBS layer was set to carry net positive charges with a density of 10 μC/m^2 on its surface, while an equal amount of negative charges was assigned to the upper electrode. The whole system was assumed to be in air, and the potential of the bottom electrode was set to zero. The electric field under open-circuit conditions was thus computed using the electrostatics module. Figure 4A shows the potential distribution of the fiber as the upper electrode moves away from the SEBS layer. The maximum value of the distance is set 0.33 mm based on the fiber's dimension without any external mechanical stimuli. The potential at the upper electrode shows a significant change with the increasing distance, which provides the driving force for current flow between the two electrodes once a circuit is built in between.

In Fig. 4B, we show the theoretical model for the fiber device, where the thickness and dielectric constant of the SEBS layer are defined as d and ε_r, and the distance between the two triboelectric parts is labeled as $x(t)$. Q represents the generated triboelectric charges, and ΔQ means the amount of transferred charges between the two electrodes once they are short-circuited. Because electrode 1 plays the role of both the triboelectric layer and electrode, its total amount of charges is $-Q_0 + \Delta Q$. By assuming that the two electrodes are infinitely large, the voltage drop ΔV from electrode 2 to electrode 1 can be deduced

$$\Delta V = \left(\frac{Q_0 - \Delta Q}{2\varepsilon_0} + \frac{Q_0}{2\varepsilon_0} - \frac{\Delta Q}{2\varepsilon_0}\right)x(t) + \left(\frac{Q_0 - \Delta Q}{2\varepsilon_0\varepsilon_r} - \frac{Q_0}{2\varepsilon_0\varepsilon_r} - \frac{\Delta Q}{2\varepsilon_0\varepsilon_r}\right)d = \frac{Q_0 - \Delta Q}{\varepsilon_0}x(t) - \frac{\Delta Q}{\varepsilon_0\varepsilon_r}d \tag{2}$$

As the charge transfer reaches equilibrium, namely, $\Delta V = 0$, then we can get

$$\frac{\Delta Q}{Q_0} = \frac{\varepsilon_r x(t)}{\varepsilon_r x(t) + d} \tag{3}$$

The relationship between $\Delta Q/Q_0$ and $x(t)$ was thus extracted on the basis of our fiber characteristics [ε_r = 2.45 (*47*), d = 50 μm]. As shown in Fig. 4B, the amount of transferred charges increases sharply with the increased distance due to the relatively large dielectric constant of SEBS [the slop for $x(t) = 0$ is equal to ε_r/d], but the derivative tends to reduce as the distance is larger than 200 μm. In our fiber structure, the gap between the two triboelectric parts was designed to be larger than 300 μm to guarantee a large amount of charge transfer (more than 90% of the total charges) between the two electrodes and thus high electrical outputs.

To quantitatively evaluate the fibers' energy harvesting performance, we characterized their outputs triggered by a cyclic vertical

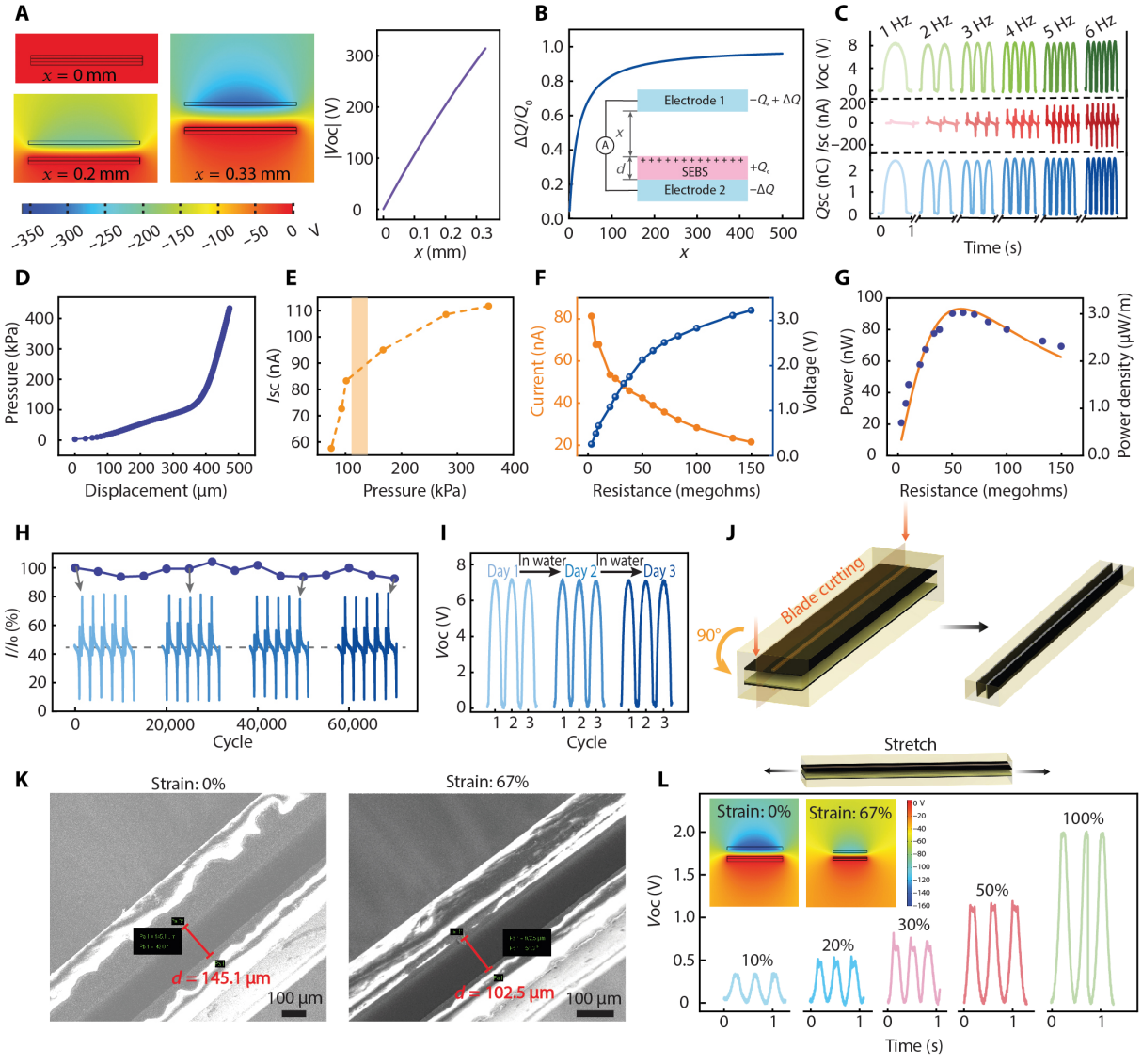

Fig. 4. Electrical characterization of the triboelectric fibers. (**A**) Numerical calculations of the potential distributions at different distances (*x*) between the two triboelectric surfaces and calculated voltages versus *x*. (**B**) Relationship between $\Delta Q/Q_0$ and *x*. (**C**) Electrical responses of the microtextured fibers under pressing with different frequencies. The fiber is 2.3 mm in width, 1.4 mm in thickness, and 3 cm in effective length. (**D**) Compressing pressure versus displacement. (**E**) Dependence of I_{SC} on compressing pressure. The shaded region highlights the pressures of 110 to 140 kPa that are high enough to trigger the gradual contact of the triboelectric surfaces. (**F** and **G**) The output as the fiber is connected to various resistors. (**H**) Long-term output stability under continuous pressing for 70,000 cycles. (**I**) Comparison of the fiber's output before and after being immersed in water for 1 and 2 days. The fiber was tested directly without further drying after being taken out from water. (**J**) Schematic showing the sample preparation for in situ SEM characterization. (**K**) In situ SEM images of a fiber with 0 and 67% elongation strain. (**L**) V_{OC} of the fiber under various repeated stretching and release movements. Inset shows the effects of mechanical stretching to the electric potential distribution.

compressive force of 6 N, driven by a custom-made DC motor. In Fig. 4C, we show typical output signals of short fibers (contact length, 3 cm) with microtextured triboelectric surfaces under various compression frequencies. While the open-circuit voltage (8.5 V, 283 V/m) and the short-circuit transferred charge (2.5 nC, 83 nC/m) remain unchanged, the short-circuit current increases linearly with the frequencies, as shown in fig. S7. By comparison, we find that the signals of the microtextured fiber are approximately double the ones with smooth surfaces (fig. S8), indicating the enhancing effect of the microstructured surfaces on the electrical performance. In table S3, we summarized the dimensions, materials, stretchability, and calibrated electrical output per unit fiber length. From the list, we can conclude that the thermally drawn fibers with sophisticated architectures show comparable electrical output performance to state-of-the-art TENG fiber devices and substantially surpass other contact-separation systems in terms of not only fabrication process and mechanical resilience but also electrical performance.

Next, we investigated the impact of structural deformation on the fiber's output performance under compression. In Fig. 4D, we show the cross-sectional displacement of a fiber under the application of a controlled compression force ramp. It is observed that the pressure increases more sharply as the displacement reaches 350 to

400 μm, which is due to the high stiffness of the structure as the two inner surfaces come into contact. The corresponding pressure at this critical region is around 110 to 140 kPa. Afterward, we recorded the output current signal under various compression pressures. As shown in Fig. 4E, the current increases linearly with the pressure before reaching a critical region, beyond which the increase tends to slow down and reaches a plateau at higher pressures. It indicates that once the two triboelectric surfaces are fully in contact, a higher force can no longer contribute to a higher signal. The standard linear relationship between the current and pressure indicates the potential of the fiber construct as a self-powered pressure sensor.

The output power of the fiber device was studied by externally connecting various resistors ranging from 3 to 150 megohms in series. The output current, voltage, and calculated power are shown in Fig. 4 (F and G). By fitting the experimental data, we observe that the fiber reaches its maximum instantaneous output power density of 3 μW/m at the load resistance of around 58 megohms. To evaluate the endurance of the fiber when subjected to long-term mechanical deformations, we imposed repeated compression and relaxation stimulation at 2 Hz while simultaneously recording the current waveforms (Fig. 4H). The current magnitude after 70,000 cycles remains 93% of its initial value. As we have discussed, we selected a stretchable and waterproof encapsulating material to guarantee the proper function of the fiber in water or under high humidity conditions. To confirm this design, we immersed the fiber in water after sealing the cavity at both extremities and recorded its voltage output before and after immersion for a few days. The stable waveforms in Fig. 4I indicate the good tolerance of the fiber construct to water infiltration. Previous studies have shown that triggered by stretching, a single-electrode fiber consisting of a silicone rubber sheath and stainless-steel yarn can generate electricity in water (*24*). Here, we realize an advanced contact-separation mode fiber integrating a water repellent encapsulating elastomer and microengineered elements, enabling the combination of both high output performance and long-term robustness in humid environment.

In addition to an increased specific surface area brought using nano/microscale structures, exploiting multilayer architectures with several TENG devices in parallel or in series is another strategy to enhance the harvested energy. The versatility of the thermal drawing process allows the realization of fibers with complex multilayer architectures that are very hard to achieve with common fabrication techniques. The cross section of the fiber we propose is shown in fig. S9A. As indicated by the dashed lines, the device can be divided into two parts, each integrating a structure studied above. By connecting these two functional parts in parallel, the output signals almost doubled compared to a single part triggered by repeated compressive force (fig. S9B).

Having assessed the electrical performance of various fibers from mechanical compression, we now explore their capability of generating electricity from stretching, another important mode of deformation. We anticipated that proper stretching can change the distance separation between the two triboelectric surfaces and thus generate electrical signals. However, the encapsulation of the fiber's hollow channel is formed by elastomers with very different mechanical properties. Therefore, it is challenging to precisely calculate the dimensional response of the channel upon stretching. To measure this response experimentally, our strategy is to cut a fiber along its longitudinal direction and then perform in situ SEM of its cross section to directly observe the change of the spacing between the two triboelectric parts upon tensile strain (Fig. 4J). From Fig. 4K, we observe that the original distance was ~145.1 μm and reduced to ~102.5 μm at 67% strain. On the basis of this finding, we performed finite element analysis in COMSOL to simulate the change of the fiber's electric potential distribution upon stretching. The charge density of the triboelectric layers was assigned on the basis of the areal change during the deformation to comply strictly with the charge conservation principle. The detailed parameters we set for this simulation are listed in table S4. The inset in Fig. 4L reveals the change of the electric field surrounding the fiber structure induced by stretching. The effect is not as noticeable as in the case of compression due to the weaker effect of structural change imposed by stretching. To confirm this response, we subjected the fiber to repeated stretching and relaxation deformation with different strains. As shown in Fig. 4L, the magnitude of the measured voltage increases with the elongation of the fiber, and the response is weaker than in the case of pressure yet remains very good to sense and generate electricity from stretching.

Long fibers and textiles that generate electricity from deformations

Now, we turn to illustrate the capability to integrate the stretchable TENG fibers with commercial fabrics for their potential use in wearable electronics or functional textiles. For this purpose, we integrated a 10-m-long continuous fiber in a serpentine pattern on a stretchable fabric with dimensions of 67 cm by 43 cm (Fig. 5A). We stretched the fabric along the longitudinal direction with a displacement of 4 cm and generated a voltage of 15 V (Fig. 5B). To show the robustness of the assembly, we compressed the fiber at various positions with an effective contact length of 5 cm and a similar force and obtained a homogeneous response (Fig. 5C).

Afterward, we arranged the single and continous fiber in a more compact way, still in a serpentine pattern, but with smaller gap distance between adjacent rows. As always, electrical contacts were made only at the two fiber ends. We then applied stronger cyclic compression to the fiber using different weights and human motions. We take the mean values of the positive and negative currents for illustration. We hand compressed the fiber with different forces, as shown in the inset of Fig. 5D. A gentle tapping triggers an output of 15 μA. By increasing the compression pressure, the average value achieves 65 μA and then as high as 230 μA. We also lifted blocks with weights of 1, 2, and 5 kg, respectively, for around 2 cm above the fiber and then allow the blocks freely fall on the fiber while recording the generated electrical waveforms, as shown in Fig. 5E. As the weight and contact area increases, the output current increases from approximately 30 to 60 μA and then 85 μA, and the V_{OC} increases from 130 to 220 V to reach 350 V. The ultimate stimulation force and contact area were applied by jumping on the fibers. The generated V_{OC} signals are beyond of the scope of our data collecting system of 550 V. The recorded current is as high as 275 μA for both positive and negative directions (Fig. 5F). Note that as we implemented this series of characterizations, the fiber had experienced a 16-month shelf storage under ambient conditions. This verifies once again the durability and robustness of the fiber devices. Moreover, the fabrication approach we propose relies on a process that regularly industrially produces up to several thousands of kilometers of fiber length. Triboelectric fibers produced at this scale could be integrated into a hundreds-of-square-meters triboelectric textile that could potentially generate much higher current, at a foreseeable ampere

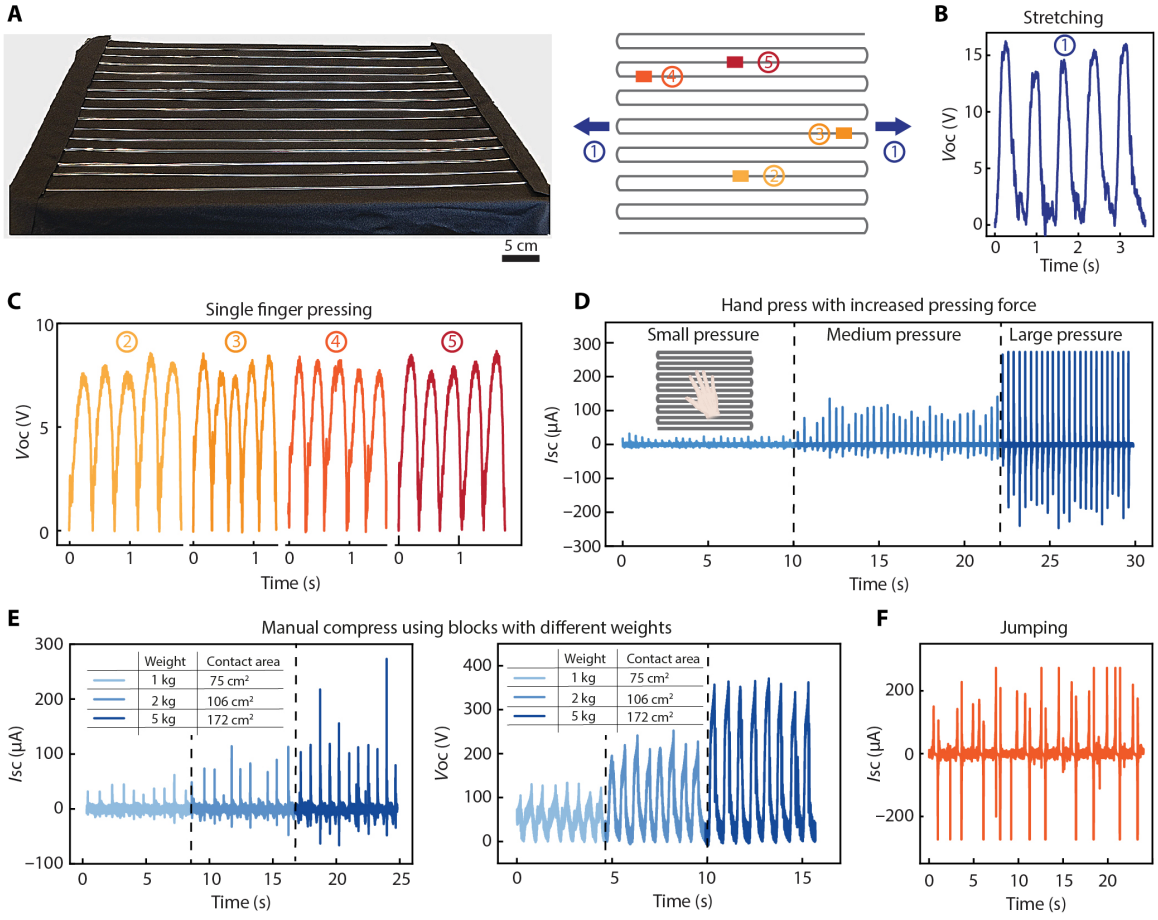

Fig. 5. Electrical output characterizations of long fibers. (**A**) Photograph of a continuous 10-m-long triboelectric fiber is integrated in a serpentine pattern on the surface of a stretchable fabric. The right schematic indicates the triggering mode for (B) and (C). (**B** and **C**) Open-circuit voltage of the long stretchable fiber triggered by a stretch along the longitudinal direction of the fabric and compressions at different positions. (**D** to **F**) Electrical outputs of the long fiber triggered by hand compression with increased foce (D), free fall of blocks with varied weights and surface areas (E), and jumping of a male researcher in our group (F).

level, under similar testing conditions. In the case of fibers with such an extreme length, a high working efficiency can be ensured by cutting the fiber and adding more contact points along the fiber length. We believe that, by coupling modern power management technologies designed for TENG devices, large-scale triboelectric fibers and textiles could make notable improvements toward various emerging soft electronics and wearable technologies.

DISCUSSION

In this work, we proposed conceptual advances to fiber-based energy harvesting systems in the aspects of materials, processes, and device designs. Specifically, we developed a highly soft and stretchable microstructured triboelectric fiber that integrates all the necessary functional components for contact-mode operation, including two triboelectric parts and an encapsulated large gap in between, within a water-repellent elastomeric cladding. We performed FEM simulations on the structure of the demonstrated fiber system to study its deformation under compression. By using the experimentally validated FEM, we explored the level of control and engineering on the mechanical behavior of the fiber that can be achieved on the basis of application-targeted designs. We proposed advanced design unachievable at these scale and feature sizes with other fabrication approaches, which integrated microstructured surfaces and staggered triboelectric components in a single thin fiber. Working in the contact-separation mode, the produced fiber can harvest energy from a variety of mechanical deformations, including compression and stretching. Moreover, the excellent deformability and robust performance of the long fibers allow the functionalization of large area textiles and enable energy harvesting and sensing with multiple modes of mechanical activation. This work brings innovative solutions to the scientific and technological challenges facing the field of TENG devices and advanced fibers and opens novel opportunities in energy harvesting, sensing, soft electronics, and smart textiles.

MATERIALS AND METHODS

Fiber fabrication

All the preforms used here have a rectangular shape with a length of 170 mm, a width of 24 mm, and a varied height depending on the elements in the preform. First, granules of the polymers were hot-pressed (Lauffer Pressen UVL 5.0 or Maschinenfabrik Herbert Meyer GmbH APV-2525/16) into geometrically defined plates. The stretchable conductive composite was fabricated with a microextruder

with twin conical screws. To obtain the 6% CNT/34% high-density polyethylene (HDPE)/60% SEBS composite, 0.8 g of 15% CNT/85% HDPE granules and 1.2 g of SEBS granules were fed into the extruder for each mixing. The extruding temperature was set at 240°C, and the rotation speed was 100 rpm. The resulting conductive filaments were cut into short rods for hot press. Then, the different polymer parts were assembled into a preform, where machined polytetrafluoroethylene (PTFE) plates with predesigned dimensions were placed at the center to create the hollow channel, and two metal rods were placed next to the composite parts to make empty channels. The preform was consolidated in the hot press at 140°C for 10 min, and the PTFE and metal rods were subsequently mechanically removed. Last, the preforms were drawn into long fibers with a custom draw tower at 215°C. To make the fibers with microtextures on the two inner triboelectric surfaces, a pretextured PDMS mold was used as the template to imprint its patterns onto CNT/HDPE/SEBS composite and Geniomer films. It was completed by hot pressing at 140°C for 5 min.

Materials characterization

The sessile drop contact angle measurement was performed through the Drop Shape Analyzer. Tested polymer films were carefully cleaned before the tests because contact angles are extremely sensitive to contamination. At least five drops were analyzed for each liquid to obtain an average contact angle value. The WVTR of SEBS was tested with a water vapor permeation analyzer at the RH of 50%. Measurements at different temperatures from 15° to 45°C were carried out to extract the activation energy of water vapor permeation for SEBS. SEM was performed on a Zeiss Merlin field emission SEM with an acceleration voltage of 3 or 4 kV using the In-Lens detector and Analytic Column Mode. The fiber samples for SEM characterizations were prepared by immersing them into liquid nitrogen for 1 min, followed by an immediate cutting at room temperature. Before characterization, the samples were coated with 10- and 5-nm Au film, respectively. The effective length of the fiber sample for the in situ tensile testing in SEM was 12 mm, and the maximum extension was 8 mm.

Mechanical and electrical tests

The mechanical tensile tests were conducted on a universal testing machine series LFM-125 kN (Walter + Bai AG) with the tensile mode (1-kN load cell). Five tests were recorded for each material. The Young's modulus was determined through a linear fitting on the stress-strain curves in the region below 3% strain (within the linear regime). The resistance values were recorded using an electrical testing instrument (Keithley SourceMeter 2450) in four-probe mode. The electrical connection for the tested fibers was realized by partially inserting metallic wires into the liquid metal channels, followed by sealing with epoxy. Both the two extremities of the fiber were well sealed for the waterproofness test of the fiber in case water flows into the channel that separates the two triboelectric parts. For the electrical output measurements of the fiber devices, a programmable electrometer (Keithley model 6517) was used to record all the signals. The data were collected and recorded by the Digilent Analog Discovery and computer-controlled software written in LabVIEW. A custom setup composed of DC motors was used to apply cyclic pressing and stretching force to the tested fibers. A force-sensitive resistor was attached to the DC motor for cyclic pressing to sense the applied compression force to the fiber sample. Before use, the resistor was calibrated with a dynamic mechanical analysis (DMA) instrument (TA Instrument DMA Q800). The relationship between the applied force and displacement of the fibers under compression was measured using the DMA, where the fibers were compressed between the top (15 mm) and bottom (30 mm) plates. The fiber lengths are between 3.6 and 4.9 cm. The loading speed was set to 5 N/mm. There was no liquid metal in the channels during the DMA tests.

Finite element modeling

FEM was performed using the commercial software package Abaqus/Explicit. The fiber was simplified to a 2D (plane-stress) model of its cross section (fig. S1) in consideration of the uniformity along its length. The geometry of the fiber cross section was built upon the fiber's optical microscopy image (fig. S1) by keeping the key features to ensure the fidelity of our FEM. Some minor features with negligible influence on the fiber deformation have been simplified or neglected to reduce the complexity of the model and computational costs (e.g., the two liquid metal channels). The width and height of the open channel were varied according to the values of x_1/x_0 and y_1/y_0 explored in Fig. 2. The structure was discretized by CPS4R plane-stress elements with an element size of ~8 μm, which was sufficiently fine confirmed by a mesh convergence study.

SEBS under large deformation exhibited nonlinear mechanical behavior, which was described by the isotropic incompressible Yeoh hyperelastic model with material constants $C1 = 482.2 \pm 1.8$ kPa, $C2 = -82.8 \pm 2.2$ kPa, and $C3 = 11.3 \pm 0.8$ kPa characterized experimentally in (*32*). The composite electrodes in the fiber were much stiffer than the SEBS, thus assumed to deform in the linear regime with a Young's modulus of 115 MPa, determined from tensile tests in Fig. 3E, and a Poisson's ratio of 0.46.

During loading, the fiber was compressed by prescribing the displacement of the top surface from 0 to 550 μm in 10 ms in a smooth step, with the lateral displacements constrained. The bottom surface of the fiber was fixed. Geometric nonlinearities were taken into consideration throughout the simulations. The contact between any two surfaces and the self-contact was assumed to be hard with no penetration and friction. We monitored the kinetic energy of the system, which was less than 0.1% of the strain energy. Hence, the simulations captured the mechanical behavior of the fiber under quasi-static loading conditions.

SUPPLEMENTARY MATERIALS

Supplementary material for this article is available at https://science.org/doi/10.1126/sciadv.abo0869

REFERENCES AND NOTES

1. S. A. Hashemi, S. Ramakrishna, A. G. Aberle, Recent progress in flexible-wearable solar cells for self-powered electronic devices. *Energ. Environ. Sci.* **13**, 685–743 (2020).
2. B. J. Kim, D. H. Kim, Y. Y. Lee, H. W. Shin, G. S. Han, J. S. Hong, K. Mahmood, T. K. Ahn, Y. C. Joo, K. S. Hong, N. G. Park, S. Lee, H. S. Jung, Highly efficient and bending durable perovskite solar cells: Toward a wearable power source. *Energ. Environ. Sci.* **8**, 916–921 (2015).
3. S. Pan, Z. Yang, P. Chen, J. Deng, H. Li, H. Peng, Wearable solar cells by stacking textile electrodes. *Angew. Chem.* **126**, 6224–6228 (2014).
4. L. K. Allison, T. L. Andrew, A wearable all-fabric thermoelectric generator. *Adv Mater Technol.* **4**, 1800615 (2019).
5. S. J. Kim, J. H. We, B. J. Cho, A wearable thermoelectric generator fabricated on a glass fabric. *Energ. Environ. Sci.* **7**, 1959–1965 (2014).
6. K. Dong, X. Peng, Z. L. Wang, Fiber/fabric-based piezoelectric and triboelectric nanogenerators for flexible/stretchable and wearable electronics and artificial intelligence. *Adv. Mater.* **32**, 1902549 (2020).

7. Q. Zheng, Y. Zou, Y. Zhang, Z. Liu, B. Shi, X. Wang, Y. Jin, H. Ouyang, Z. Li, Z. L. Wang, Biodegradable triboelectric nanogenerator as a life-time designed implantable power source. *Sci. Adv.* **2**, e1501478 (2016).
8. Q. Zheng, H. Zhang, B. Shi, X. Xue, Z. Liu, Y. Jin, Y. Ma, Y. Zou, X. Wang, Z. An, W. Tang, W. Zhang, F. Yang, Y. Liu, X. Lang, Z. Xu, Z. Li, Z. L. Wang, In vivo self-powered wireless cardiac monitoring via implantable triboelectric nanogenerator. *ACS Nano* **10**, 6510–6518 (2016).
9. Q. Zheng, B. Shi, F. Fan, X. Wang, L. Yan, W. Yuan, S. Wang, H. Liu, Z. Li, Z. L. Wang, In vivo powering of pacemaker by breathing-driven implanted triboelectric nanogenerator. *Adv. Mater.* **26**, 5851–5856 (2014).
10. H. Guo, X. Pu, J. Chen, Y. Meng, M. H. Yeh, G. Liu, Q. Tang, B. Chen, D. Liu, S. Qi, C. Wu, C. Hu, J. Wang, Z. L. Wang, A highly sensitive, self-powered triboelectric auditory sensor for social robotics and hearing aids. *Sci. Robot.* **3**, eaat2516 (2018).
11. T. Jin, Z. Sun, L. Li, Q. Zhang, M. Zhu, Z. Zhang, G. Yuan, T. Chen, Y. Tian, X. Hou, C. Lee, Triboelectric nanogenerator sensors for soft robotics aiming at digital twin applications. *Nat. Commun.* **11**, 5381 (2020).
12. J. Luo, Z. Wang, L. Xu, A. C. Wang, K. Han, T. Jiang, Q. Lai, Y. Bai, W. Tang, F. R. Fan, Z. L. Wang, Flexible and durable wood-based triboelectric nanogenerators for self-powered sensing in athletic big data analytics. *Nat. Commun.* **10**, 5147 (2019).
13. J. Luo, W. Gao, Z. L. Wang, The triboelectric nanogenerator as an innovative technology toward intelligent sports. *Adv. Mater.* **33**, 2004178 (2021).
14. X. Chen, X. Xie, Y. Liu, C. Zhao, M. Wen, Z. Wen, Advances in healthcare electronics enabled by triboelectric nanogenerators. *Adv. Funct. Mater.* **30**, 2004673 (2020).
15. X. He, H. Zou, Z. Geng, X. Wang, W. Ding, F. Hu, Y. Zi, C. Xu, S. L. Zhang, H. Yu, M. Xu, W. Zhang, C. Lu, Z. Lin Wang, A hierarchically nanostructured cellulose fiber-based triboelectric nanogenerator for self-powered healthcare products. *Adv. Funct. Mater.* **28**, 1805540 (2018).
16. G. Zhao, J. Yang, J. Chen, G. Zhu, Z. Jiang, X. Liu, G. Niu, Z. L. Wang, B. Zhang, Keystroke dynamics identification based on triboelectric nanogenerator for intelligent keyboard using deep learning method. *Adv. Mater. Technol.* **4**, 1800167 (2019).
17. S. L. Zhang, D. J. Roach, S. Xu, P. Wang, W. Zhang, H. J. Qi, Z. L. Wang, Electromagnetic pulse powered by a triboelectric nanogenerator with applications in accurate self-powered sensing and security. *Adv. Mater. Technol.* **5**, 2000368 (2020).
18. A. Canales, X. Jia, U. P. Froriep, R. A. Koppes, C. M. Tringides, J. Selvidge, C. Lu, C. Hou, L. Wei, Y. Fink, P. Anikeeva, Multifunctional fibers for simultaneous optical, electrical and chemical interrogation of neural circuits in vivo. *Nat. Biotechnol.* **33**, 277–284 (2015).
19. T. Nguyen-Dang, A. C. de Luca, W. Yan, Y. Qu, A. G. Page, M. Volpi, T. Das Gupta, S. P. Lacour, F. Sorin, Controlled sub-micrometer hierarchical textures engineered in polymeric fibers and microchannels via thermal drawing. *Adv. Funct. Mater.* **27**, 1605935 (2017).
20. G. Loke, T. Khudiyev, B. Wang, S. Fu, S. Payra, Y. Shaoul, J. Fung, I. Chatziveroglou, P. Chou, I. Chinn, W. Yan, A. Gitelson-kahn, J. Joannopoulos, Y. Fink, Digital electronics in fibres enable fabric-based machine-learning inference. *Nat. Commun.* **12**, 3317 (2021).
21. X. Shi, Y. Zuo, P. Zhai, J. Shen, Y. Yang, Z. Gao, M. Liao, J. Wu, J. Wang, X. Xu, Q. Tong, B. Zhang, B. Wang, X. Sun, L. Zhang, Q. Pei, D. Jin, P. Chen, H. Peng, Large-area display textiles integrated with functional systems. *Nature* **591**, 240–245 (2021).
22. J. He, C. Lu, H. Jiang, F. Han, X. Shi, J. Wu, L. Wang, T. Chen, J. Wang, Y. Zhang, H. Yang, G. Zhang, X. Sun, B. Wang, P. Chen, Y. Wang, Y. Xia, H. Peng, Scalable production of high-performing woven lithium-ion fibre batteries. *Nature* **597**, 57–63 (2021).
23. M. Liao, C. Wang, Y. Hong, Y. Zhang, X. Cheng, H. Sun, X. Huang, L. Ye, J. Wu, X. Shi, X. Kang, X. Zhou, J. Wang, P. Li, X. Sun, P. Chen, B. Wang, Y. Wang, Y. Xia, Y. Cheng, H. Peng, Industrial scale production of fibre batteries by a solution-extrusion method. *Nat. Nanotechnol.* **17**, 372–377 (2022).
24. W. Gong, C. Hou, J. Zhou, Y. Guo, W. Zhang, Y. Li, Q. Zhang, H. Wang, Continuous and scalable manufacture of amphibious energy yarns and textiles. *Nat. Commun.* **10**, 868 (2019).
25. X. He, Y. Zi, H. Guo, H. Zheng, Y. Xi, C. Wu, J. Wang, W. Zhang, C. Lu, Z. L. Wang, A highly stretchable fiber-based triboelectric nanogenerator for self-powered wearable electronics. *Adv. Funct. Mater.* **27**, 1604378 (2017).
26. X. Yu, J. Pan, J. Zhang, H. Sun, S. He, L. Qiu, H. Lou, X. Sun, H. Peng, A coaxial triboelectric nanogenerator fiber for energy harvesting and sensing under deformation. *J. Mater. Chem. A* **5**, 6032–6037 (2017).
27. Y. Cheng, X. Lu, K. Hoe Chan, R. Wang, Z. Cao, J. Sun, G. Wei Ho, A stretchable fiber nanogenerator for versatile mechanical energy harvesting and self-powered full-range personal healthcare monitoring. *Nano Energy* **41**, 511–518 (2017).
28. W. Gong, C. Hou, Y. Guo, J. Zhou, J. Mu, Y. Li, Q. Zhang, H. Wang, A wearable, fibroid, self-powered active kinematic sensor based on stretchable sheath-core structural triboelectric fibers. *Nano Energy* **39**, 673–683 (2017).
29. D. Kim, J. Park, Y. T. Kim, Core-shell and helical-structured cylindrical triboelectric nanogenerator for wearable energy harvesting. *ACS Appl. Energy Mater.* **2**, 1357–1362 (2019).
30. W. Yan, I. Richard, G. Kurtuldu, N. D. James, G. Schiavone, J. W. Squair, T. Nguyen-Dang, T. Das Gupta, Y. Qu, J. D. Cao, R. Ignatans, S. P. Lacour, V. Tileli, G. Courtine, J. F. Löffler, F. Sorin, Structured nanoscale metallic glass fibres with extreme aspect ratios. *Nat. Nanotechnol.* **15**, 875–882 (2020).
31. S. Shadman, T. Nguyen-Dang, T. das Gupta, A. G. Page, I. Richard, A. Leber, J. Ruza, G. Krishnamani, F. Sorin, Microstructured biodegradable fibers for advanced control delivery. *Adv. Funct. Mater.* **30**, 1910283 (2020).
32. A. Leber, A. G. Page, D. Yan, Y. Qu, S. Shadman, P. Reis, F. Sorin, Compressible and electrically conducting fibers for large-area sensing of pressures. *Adv. Funct. Mater.* **30**, 1904274 (2020).
33. F. Sordo, E. Janecek, Y. Qu, V. Michaud, F. Stellacci, J. Engmann, T. J. Wooster, F. Sorin, Microstructured fibers for the production of food. *Adv. Mater.* **31**, 1807282 (2019).
34. C. Dong, A. Leber, T. das Gupta, R. Chandran, M. Volpi, Y. Qu, T. Nguyen-Dang, N. Bartolomei, W. Yan, F. Sorin, High-efficiency super-elastic liquid metal based triboelectric fibers and textiles. *Nat. Commun.* **11**, 3537 (2020).
35. X. S. Zhang, J. Brugger, B. Kim, A silk-fibroin-based transparent triboelectric generator suitable for autonomous sensor network. *Nano Energy* **20**, 37–47 (2016).
36. H. Guo, J. Chen, L. Tian, Q. Leng, Y. Xi, C. Hu, Airflow-induced triboelectric nanogenerator as a self-powered sensor for detecting humidity and airflow rate. *ACS Appl. Mater. Interfaces* **6**, 17184–17189 (2014).
37. H. Zhang, Y. Yang, Y. Su, J. Chen, C. Hu, Z. Wu, Y. Liu, C. Ping Wong, Y. Bando, Z. L. Wang, Triboelectric nanogenerator as self-powered active sensors for detecting liquid/gaseous water/ethanol. *Nano Energy* **2**, 693–701 (2013).
38. Y. Qu, T. Nguyen-Dang, A. G. Page, W. Yan, T. Das Gupta, G. M. Rotaru, R. M. Rossi, V. D. Favrod, N. Bartolomei, F. Sorin, Superelastic multimaterial electronic and photonic fibers and devices via thermal drawing. *Adv. Mater.* **30**, 1707251 (2018).
39. N. G. Dhere, Flexible packaging for PV modules. *Proc. SPIE.* **7048**, 70480R (2008).
40. K. Madhavan, B. S. R. Reddy, Poly(dimethylsiloxane-urethane) membranes: Effect of hard segment in urethane on gas transport properties. *J. Memb. Sci.* **283**, 357–365 (2006).
41. A. Ferdinand, J. Springer, Gas permeability of block copolymers of styrene and butadiene. *Colloid Polym. Sci.* **267**, 1057–1063 (1989).
42. C. E. Chinma, C. C. Ariahu, J. S. Alakali, Effect of temperature and relative humidity on the water vapour permeability and mechanical properties of cassava starch and soy protein concentrate based edible films. *J. Food Sci. Technol.* **52**, 2380–2386 (2015).
43. Y. Guo, S. Jiang, B. J. B. Grena, I. F. Kimbrough, E. G. Thompson, Y. Fink, H. Sontheimer, T. Yoshinobu, X. Jia, Polymer composite with carbon nanofibers aligned during thermal drawing as a microelectrode for chronic neural interfaces. *ACS Nano* **11**, 6574–6585 (2017).
44. T. Nguyen-Dang, A. G. Page, Y. Qu, M. Volpi, W. Yan, F. Sorin, Multi-material micro-electromechanical fibers with bendable functional domains. *J. Phys. D Appl. Phys.* **50**, 144001 (2017).
45. L. Wang, J. Qiu, E. Sakai, X. Wei, Effects of multiwalled carbon nanotube mass fraction on microstructures and electrical resistivity of polycarbonate-based conductive composites. *Sci. Eng. Compos. Mater.* **24**, 163–175 (2017).
46. T. Nguyen Dang, I. Richard, E. Goy, F. Sordo, F. Sorin, Insights into the fabrication of sub-100 nm textured thermally drawn fibers. *J. Appl. Phys.* **125**, 175301 (2019).
47. R. M. Grigorescu, F. Ciuprina, P. Ghioca, M. Ghiurea, L. Iancu, B. Spurcaciu, D. M. Panaitescu, Mechanical and dielectric properties of SEBS modified by graphite inclusion and composite interface. *J. Phys. Chem. Solid* **89**, 97–106 (2016).
48. D. K. Owens, R. C. Wendt, Estimation of the surface free energy of polymers. *J. Appl. Polym. Sci.* **13**, 1741–1747 (1969).
49. M. Annamalai, K. Gopinadhan, S. A. Han, S. Saha, H. J. Park, E. B. Cho, B. Kumar, A. Patra, S. W. Kim, T. Venkatesan, Surface energy and wettability of van der Waals structures. *Nanoscale* **8**, 5764–5770 (2016).
50. F. D. Petke, B. R. Ray, Temperature dependence of contact angles of liquids on polymeric solids. *J. Colloid Interface Sci.* **31**, 216–227 (1969).
51. L. Zheng, M. Zhu, B. Wu, Z. Li, S. Sun, P. Wu, Conductance-stable liquid metal sheath-core microfibers for stretchy smart fabrics and self-powered sensing. *Sci. Adv.* **7**, eabg4041 (2021).
52. K. Dong, J. Deng, Y. Zi, Y. Wang, C. Xu, H. Zou, W. Ding, Y. Dai, B. Gu, B. Sun, Z. Wang, 3D orthogonal woven triboelectric nanogenerator for effective biomechanical energy harvesting and as self-powered active motion sensors. *Adv. Mater.* **29**, 1702648 (2017).
53. Y. Lai, H. Lu, H. Wu, D. Zhang, J. Yang, J. Ma, M. Shamsi, V. Vallem, M. D. Dickey, Elastic multifunctional liquid–metal fibers for harvesting mechanical and electromagnetic energy and as self-powered sensors. *Adv. Energy Mater.* **11**, 2100411 (2021).
54. Y. Yang, L. Xie, Z. Wen, C. Chen, X. Chen, A. Wei, P. Cheng, X. Xie, X. Sun, Coaxial triboelectric nanogenerator and supercapacitor fiber-based self-charging power fabric. *ACS Appl. Mater. Interfaces* **10**, 42356–42362 (2018).
55. Y. Tong, Z. Feng, J. Kim, J. Robertson, X. Jia, B. Johnson, 3D printed stretchable triboelectric nanogenerator fibers and devices. *Nano Energy* **75**, 104973 (2020).
56. Z. Wang, T. Wu, Z. Wang, T. Zhang, M. Chen, J. Zhang, L. Liu, M. Qi, Q. Zhang, J. Yang, W. Liu, H. Chen, Y. Luo, L. Wei, Designer patterned functional fibers via direct imprinting in thermal drawing. *Nat. Commun.* **11**, 3842 (2020).

57. M. Chen, Z. Wang, Q. Zhang, Z. Wang, W. Liu, M. Chen, L. Wei, Self-powered multifunctional sensing based on super-elastic fibers by soluble-core thermal drawing. *Nat. Commun.* **12**, 1416 (2021).

Acknowledgments: We thank the Soft Materials Laboratory (SMAL) and the Laboratory for Processing of Advanced Composites (LPAC) at EPFL for the support in terms of equipment usage. **Funding:** This work was supported by the Swiss National Science Foundation (SNSF 200021_204579) and the CCMX Challenge funding scheme in Switzerland. **Author contributions:** Conceptualization: C.D. and F.S. Methodology: C.D. Investigation: C.D., A.L., D.Y., H.B., S.L., T.D.G., and S.S. Supervision: F.S. Writing—original draft: C.D. Writing—review and editing: C.D., D.Y., P.M.R., and F.S. **Competing interests:** The authors declare that they have no competing interests. **Data and materials availability:** All data needed to evaluate the conclusions in the paper are present in the paper and/or the Supplementary Materials.

Submitted 17 January 2022
Accepted 26 September 2022
Published 11 November 2022
10.1126/sciadv.abo0869